Boundary-Layer Meteorol (2011) 141:369–391
DOI 10.1007/s10546-011-9657-6

ARTICLE

Convective Boundary-Layer Entrainment: Short Review and Progress using Doppler Lidar

K. Träumner · Ch. Kottmeier · U. Corsmeier · A. Wieser

Received: 29 October 2010 / Accepted: 20 August 2011 / Published online: 29 September 2011

Abstract The entrainment of air from the free atmosphere into the convective boundary layer is reviewed and further investigated using observations from a 2 μm Doppler lidar. It is possible to observe different individual processes entraining air into the turbulent layer, which develop with varying stability of the free atmosphere. These different processes are attended by different entrainment-zone thicknesses and entrainment velocities. Four classes of entrainment parametrizations, which describe relationships between the fundamental parameters of the process, are examined. Existing relationships between entrainment-zone thickness and entrainment velocity are basically confirmed using as scaling parameters boundary-layer height and convective velocity. An increase in the correlation coefficient between stability parameters based on the stratification of the free atmosphere and entrainment velocity (and entrainment-zone thickness respectively) up to 200% was possible using more suitable length and velocity scales.

Keywords Convective boundary layer · Doppler lidar · Entrainment

1 Introduction

Entrainment describes the process of mixing a non-turbulent fluid into a turbulent fluid to such an extent that the former non-turbulent fluid becomes a part of the turbulent region afterwards. It is a problem that has been addressed for more than 50 years (Turner 1986) in fluid mechanics and in meteorology, where entrainment is investigated in the context of the atmospheric boundary layer and clouds. Here, a simple case of stratified fluids in the atmosphere is examined—the cloudless convective boundary layer.

In particular under the influence of an anticyclone, the atmospheric boundary layer typically follows well-known daily cycles: slow growth in the morning, through to dissolution

K. Träumner (✉) · Ch. Kottmeier · U. Corsmeier · A. Wieser
Karlsruhe Institute of Technology, Institute for Meteorology and Climate Research,
Hermann-von-Helmholtz-Platz 1, Eggenstein-Leopoldshafen, Germany
e-mail: katja.traeumner@kit.edu

of the stable layer from the previous night, is followed by rapid growth and a nearly constant height in the late afternoon. In general, the convective boundary-layer growth is driven by a complex interaction of turbulent heat and moisture fluxes, synoptic-scale vertical motion, the stability of the interface between the turbulent boundary layer and the free atmosphere and of the free atmosphere itself and, of course, by entrainment processes mixing potentially warmer and less moist air from the free atmosphere into the convective boundary layer. Additionally, the boundary-layer evolution of the previous day, local wind systems, terrain effects, advection as well as clouds influence the process.

Based on the growth of the turbulent layer, an entrainment velocity w_e is defined

$$w_e = \frac{dh}{dt} - w_L \tag{1}$$

with boundary-layer height, h, and synoptic-scale vertical motion, w_L. The second fundamental parameter associated with the entrainment process is the thickness of the zone between the turbulent and non-turbulent layers, the so-called entrainment zone, Δh.

There have been many atmospheric boundary-layer evolution studies in the last few decades (e.g. Deardorff et al. 1980; Boers and Eloranta 1986; Angevine et al. 1994; Davis et al. 1997; Conzemius and Fedorovich 2006). Detailed studies, especially dealing with entrainment-zone dynamics, require sophisticated measurements: high-resolution boundary-layer height measurements, detailed measurements of the entrainment-zone thickness, as well as measurements to characterize turbulence and stability throughout the boundary layer and above. Up to now previously in-situ aircraft measurements were used, which enable estimations of the entrainment flux and the jump of temperature and humidity across the inversion layer (e.g. Flamant et al. 1997; Lenschow et al. 1999; Canut et al. 2010), but they do not allow fine measurements of the boundary-layer growth or turbulence throughout the whole boundary layer. These needs can be satisfied with lidar measurements, which, in turn, are up to now not able to measure temperature fluxes. Provided that there is enough aerosol in the atmosphere, Doppler lidar gives the possibility to visualize the processes associated with entrainment using the aerosol backscatter signal on the one hand, and to characterize the turbulence using high-resolution wind measurements throughout the whole boundary layer on the other hand. This approach provides a new insight into entrainment.

Additionally there is a growing demand for new parametrizations to describe the convective boundary-layer growth in high-resolution mesoscale and climate models. Based on the new measurement technique and the need of parameters, this study discusses the "old" problem of convective boundary-layer development and presents new results, which lead to a better understanding of the entrainment process.

In the next section, a short review covering empirical results concerning entrainment in the framework of the convective boundary layer is given. This includes individual processes responsible for mixing a non-turbulent fluid into a turbulent fluid, scales in the boundary layer as well as empirical results of different types of parametrizations from former studies. This short review does not cover entrainment models, because many good reviews in this context exists, e.g. Tennekes and Driedonks (1981), Van Zanten et al. (1999), and Conzemius and Fedorovich (2006). Also the review does not address the stratocumulus-topped boundary layer, although field studies and simulations in this area contribute much understanding to convective boundary-layer entrainment. An overview of the stratocumulus-topped boundary layer is given e.g. by Moeng (1998). In Sect. 3, the experimental set-up and the data processing are described. Two concepts of boundary-layer height and two concepts of entrainment-zone thickness will be introduced as well as two sets of scales. In Sect. 4, entrainment regimes

in the convective boundary layer, identified by means of lidar measurements, are presented. In addition, different parametrizations are re-examined, placing special attention on their behaviour using different scales. Finally, conclusions are given in Sect. 5.

2 Entrainment: Short Review of Empirical Results

2.1 Entrainment Events

Up to now, details of small-scale processes associated with entrainment have been examined previously in laboratory tank experiments and numerical simulations (e.g. Carruthers and Hunt 1986; McGrath et al. 1997; Sullivan et al. 1998). First attempts to visualize processes in the atmospheric boundary layer were done by aircraft measurements, e.g. Couvreux et al. (2007) and Canut et al. (2010), both in the convective boundary layer, as well as Nicholls and Turton (1986) and Lenschow et al. (2000b) in the stratocumulus-topped boundary layer. But these field measurements were not able to resolve details of individual processes, comparable to the laboratory experiments or simulations.

Four distinct mechanisms are assumed to entrain fluid into a turbulent layer:

(i) Non-turbulent fluid can be enclosed by the turbulent fluid and incorporated into the turbulent flow by turbulent straining until mixing at molecular scales occurs. An entrainment process described as entrainment between domes caused by overshooting parcels (Boers and Eloranta 1986) is associated with this so-called large-scale engulfment.
(ii) Shear instabilities generated by different wind regimes in the turbulent and non-turbulent regions (Kim et al. 2003) or by eddies travelling parallel to the inversion layer (Hunt 1998) induce breaking Kelvin-Helmholtz and Hölmböe waves (Strang and Fernando 2001).
(iii) Impinging convective eddies (Linden 1973) and buoyancy plumes (Baines 1975) can distort the interface between the turbulent and the non-turbulent layers. Entrainment by thin filaments is expected to occur during the recoil process of the distortion or at the edges of the deformation (Sullivan et al. 1998).
(iv) Turbulent eddies can excite wave motions in stratified layers (Dohan and Sutherland 2003). Resonant modes of these internal waves can grow, break intermittently, and cause entrainment (Carruthers and Moeng 1987; Hannoun and List 1988).

Which one of the above mechanisms dominates the entrainment depends on conditions in the fluids and at the interface between the turbulent fluid and non-turbulent one. A widely used parameter to describe these conditions is a Richardson number,

$$Ri(L, V) = \Delta b \frac{L}{V^2}, \tag{2}$$

where $\Delta b = g\Delta\rho/\rho \approx g\ \Delta\theta/\theta$ is the buoyancy difference across the interface, L is a characteristic length scale and V is a characteristic velocity scale.

2.2 Scales Associated with Entrainment

To describe the entrainment process, different scales are used to create dimensionless groups, e.g. $\Delta h/L$, w_e/V, and Ri. For the velocity scale, commonly the discrimination depends on the turbulence generating process: a purely convective regime is described by the convective velocity $w_* = \left(g\ h\ \overline{w'\theta'_V}_0/\overline{\theta_V}\right)^{1/3}$, with the turbulent virtual potential temperature flux at

the ground, $\overline{w'\theta'_V}_0$, and the mean virtual potential temperature in the convective boundary layer, $\overline{\theta_V}$ (Deardorff 1970). Turbulence generated by the near-surface wind shear is represented by the friction velocity $u_{*,0} = \left(\overline{u'w'}_0^2 + \overline{v'w'}_0^2\right)^{1/4}$, and boundary-layer top shear stress is associated with the velocity difference across the entrainment zone, ΔV. Multiple driving processes are considered using a combined scale of w_*, $u_{*,0}$ and ΔV (Deardorff 1983; Pino et al. 2003; Kim et al. 2006; Conzemius and Fedorovich 2006). The so-called top-down velocity scale, introduced by Sorbjan (1990), $W_* = \left(g\ h\ \overline{w'\theta'_V}_h / \overline{\theta_V}\right)^{1/3}$ with the turbulent virtual potential temperature flux at the interface between the convective boundary layer and the free atmosphere, $\overline{w'\theta'_V}_h$, as well as the use of the standard deviation of the vertical wind velocity, σ_w (Tennekes 1973), or the horizontal wind velocity, σ_u (Hannoun and List 1988; Fernando and Hunt 1996, 1997; Strang and Fernando 2001) in the turbulent layer are further attempts to consider simultaneously different turbulence generating processes. A more descriptive velocity scale should be mentioned for completeness: the mean vertical velocity of the convective plumes.

For the length scale, essentially two parameters are common: h (Deardorff et al. 1980; Boers and Eloranta 1986; Fedorovich et al. 2004) and the vertical or horizontal integral length scale, l, (Lenschow and Stankov 1986; Hannoun and List 1988; Fernando and Hunt 1996; Strang and Fernando 2001). Other conceivable length scales are the wavelength of the maximum of the product of the velocity spectra and the wavenumber (Caughey and Palmer 1979), and the Obukhov length (Monin and Obukhov 1954), which characterizes the dynamic sublayer. Again, as an intuitive length scale directly describing turbulence, geometrical parameters of plumes are conceivable.

Here, two combinations of length and velocity scale, (L, V), are of special interest: (h, w_*), and $(l, \sigma_{\mathrm{w,max}})$, where $\sigma_{\mathrm{w,max}}$ is the maximum standard deviation of vertical velocity in the turbulent boundary layer. The pair (h, w_*) is from now on referred to as the conventional combination, because it is widely used in convective boundary-layer research. The pair $(l, \sigma_{\mathrm{w,max}})$ is a combination relevant to entrainment studies in fluid mechanics and will be referred to hereafter as the turbulent combination, because it is expected to describe the turbulence more directly compared to (h, w_*). In the past $(l, \sigma_{\mathrm{w,max}})$ has not been used in atmospheric research, because these two quantities are difficult to measure throughout the whole atmospheric boundary layer.

The different scales can be used to define a variety of different Richardson numbers. These different definitions have to be considered comparing results concerning the occurrence of the different entrainment mechanisms described in the previous section, because the magnitude of Ri depends on the used scales (for quantitative values see e.g. Fernando and Hunt 1997; McGrath et al. 1997; Sullivan et al. 1998). For small Richardson numbers, most authors agree that the large-scale engulfment (mechanism i) dominates; for increasing Ri the mechanisms are successively Kelvin-Helmholtz waves (ii) and impinging eddies (iii), and finally breaking of internal waves (iv).

2.3 Previous Empirical Results

Four classes of parametrizations can be found in literature:

(i) "Constant-ratio-parametrizations" assume that the entrainment-zone thickness and the entrainment velocity are directly proportional to a length scale, and to a velocity scale respectively:

Table 1 Parameters for "Simple-stability-parametrizations" based on Eq. 5

Author	Kind of study	a	b	c
Deardorff et al. (1980)	Laboratory tank experiment (convective turbulence) (normalized by h_0)	1.31	1	0.21
Boers and Eloranta (1986)	Ground-based lidar in a convective boundary layer	1.57	1	0.23
Davis et al. (1997)	Aircraft-based lidar in a convective boundary layer	1.5	0.5	0
Boers (1989)	Based on data from Deardorff et al. (1980) and Boers and Eloranta (1986)	1.23	0.5	0
Nelson et al. (1989) and Gryning and Batchvarova (1994)	Based on data from Deardorff et al. (1980)		0.25	
Sullivan et al. (1998)	Large-eddy simulation convective boundary layer		1	
Fedorovich et al. (2004)	Large-eddy simulation convective boundary layer		0.5	

All of these studies use the boundary-layer height as the length scale and convective velocity as the velocity scale

$$\frac{\Delta h}{L} = \text{const.}, \tag{3}$$

$$\frac{w_\mathrm{e}}{V} = \text{const.} \tag{4}$$

These parametrizations were based e.g. on simple geometrical considerations using the first-order jump model of Haegeli et al. (2000) and a strict ratio between $\overline{w'\theta'}_h$ and $\overline{w'\theta'}_0$ (typical closure assumption, e.g. Tennekes 1973; Yi et al. 2001; although observations and simulations do not support this unrestrictedly, e.g. Angevine 2008). Also the entrainment hypothesis, that the mean inflow velocity across the edge of a turbulent flow is assumed to be proportional to a characteristic velocity (Turner 1986), supports this class of parametrizations.

(ii) "Simple-stability-parametrizations" are parametrizations using Ri as a measure of stability at the interface between the convective boundary layer and the free atmosphere:

$$\frac{\Delta h}{L} = a\,Ri^{-b} + c, \tag{5}$$

$$\frac{w_\mathrm{e}}{V} = \alpha\,Ri^{-\beta}, \tag{6}$$

with $a, b, c, \alpha, \beta > 0$. These parametrizations were based on e.g. zero-order jump models (Stull 1973; Tennekes 1973), or process based models using parcel theory (Boers 1989), impinging vortex rings (Linden 1973) and the generation of internal waves (Fernando and Hunt 1997). Whereas w_e/V vanishes for large Ri, $\Delta h/L$ often is set to a constant limit c. This is an empirical result, which says that at high stability negligible entrainment occurs (entrainment velocity is zero), but a small well-defined transition zone (entrainment zone) forms. Tables 1 and 2 summarize numerical values from previous studies.

Several authors, e.g. Deardorff (1983), Fernando (1991), Strang and Fernando (2001), and Sun and Wang (2008), argue that different entrainment regimes, linked to different entrainment processes (Sect. 2.1), need different parametrizations (Table 2).

Table 2 Parameters for "Simple-stability-parametrizations" based on Eq. 6

Author	Kind of study	α	β	V	L
Deardorff et al. (1980)	Laboratory tank experiment (convective turbulence)	0.25	1	w_*	h
Deardorff et al. (1980)	Laboratory tank experiment (convective turbulence)	1.1	1.5	w_*	h
Turner (1986)	Laboratory tank experiment (oscillating grid)		1.5	σ_u	l_u
Linden (1973)	Laboratory tank experiment (impinging vortex rings)	0.6	1.5	u_v	a_v
Baines (1975)	Laboratory tank experiment (impinging plumes)		1.5	u_p	a_p
Hannoun and List (1988)	Laboratory tank experiment (oscillating grid)		1.5	σ_u	$l_{u,w}$
Fernando (1991)	Summary laboratory tank experiment (no shear)		1–1.75	w_*	h
Fernando (1991)	Summary laboratory tank experiment (with shear)		0.9–2	u_*	h
Sullivan et al. (1998)	Large-eddy simulation convective boundary layer	0.2	1	w_*	h
Strang and Fernando (2001)	Laboratory tank experiment		0/2.6/1.3	$\Delta V, \sigma_u$	l_u
Fedorovich et al. (2004)	Large-eddy simulation convective boundary layer		1–1.5	w_*	h

The studies differ regarding the used scales (L, V). a_v (a_p) is the diameter of the examined vortex ring (convective plume) and u_v (u_p) is its velocity

(iii) "Direct-relationship-parametrizations" combine Eqs. 5 and 6:

$$\frac{\Delta h}{L} \propto \left(\frac{w_e}{V}\right)^m, \tag{7}$$

where Table 3 outlines empirical results using this relationship. The studies show linear relationships as well as values of $m < 1$. Based on the empirical results from Tables 1 and 2, $m \in [0.17; 1]$. Using ground-based aerosol lidar, Nelson et al. (1989) showed a highly time-dependent behaviour of m, as a function of the state of convective boundary-layer evolution.

(iv) "Extensive-stability-parametrizations" employ a relationship between the entrainment-zone thickness and a Richardson number using $V = w_e$:

$$Ri_{we} = g\frac{\Delta\theta}{\overline{\theta}}\frac{L}{w_e^2}. \tag{8}$$

They were proposed by Gryning and Batchvarova (1994) using parcel theory and the top-down velocity scale (and $L = h$):

$$\frac{\Delta h}{h} = 3.3\ Ri_{we}^{-1/3} + 0.2. \tag{9}$$

The concept combines all entrainment-related parameters (Δh, w_e, $\Delta\theta$) in one relation. These parametrizations are supported by sodar measurements (Beyrich and Gryning 1998).

Table 3 "Direct-relationship-parametrizations" between the normalized entrainment-zone thickness and the normalized entrainment velocity based on Eq. 7

Author	Kind of study	Relationship
Deardorff et al. (1980)	Laboratory tank experiment (convective turbulence)	$\frac{\Delta h}{h} = 0.21 + 5.24\,\frac{w_e}{w_*}$
Boers and Eloranta (1986)	Results from Deardorff et al. (1980)	$\frac{\Delta h}{h} = 0.19 + 5.35\,\frac{1}{w_*}\left(\frac{dh}{dt} - w_L\right)$
Boers and Eloranta (1986)	Ground-based lidar in a convective boundary layer	$\frac{\Delta h}{h} = 0.09 + 5.5\,\frac{1}{w_*}\left(\frac{dh}{dt}\right)$
Boers and Eloranta (1986)	Ground-based lidar in a convective boundary layer	$\frac{\Delta h}{h} = 0.005 + 5.75\,\frac{1}{w_*}\left(\frac{dh}{dt} - w_L\right)$
Deardorff et al. (1980)	Laboratory tank experiment (convective turbulence)	$\frac{\Delta h}{h} = 1.23\left(\frac{w_e}{w_*}\right)^{2/3} + 0.21$
Melfi et al. (1985)	Results from Deardorff et al. (1980)	$\frac{\Delta h}{h} \sim 3\left(\frac{w_e}{w_*}\right)^{0.5}$
Beyrich and Gryning (1998)	Ground-based sodar in a convective boundary layer	$\frac{\Delta h}{h} \propto \left(\frac{w_e}{w_*}\right)^{0.24}$
Deardorff (1983)	Results from Deardorff et al. (1980)	$\frac{\Delta h}{h} \propto \left(\frac{w_e}{w_*}\right)^{0.3}$

3 Data

3.1 Instrument Set-Up and Data Collection

A 2-μm heterodyne Doppler lidar "WindTracer" from Lockheed Martin Coherent Technologies was used to provide aerosol backscatter and radial wind velocity data. The system has a pulse length of 370 ns (56 m), a pulse repetition frequency of 500 Hz, and an average power of 1 W (4.5 kW peak power). The data were sampled in two different modes: a scanning mode, accumulating 50 pulses (effective sampling rate of 10 Hz), and a vertical stare mode, accumulating 500 pulses (effective sampling rate of 1 Hz). During both modes a range gate length of 72 m was applied. The two modes differ relating to the position of the range gate centres along the beam. Using the range-corrected signal-to-noise ratio (SNR), it is possible to obtain an aerosol backscatter coefficient. For the "WindTracer" system, a constant extinction coefficient is used, and no calibration is performed. The aerosol backscatter values thus have to be interpreted only as a qualitative measure of aerosol backscatter with higher numbers indicating higher concentrations and/or surface areas.

Based on the Doppler frequency shift due to the movement of the scatterers relative to the lidar beam, the radial wind velocity can be measured. Comparing the radial wind measurements with sonic anemometer data, Calhoun et al. (2005) have shown that the lidar wind measurements are bias free. Using the covariance technique (Frehlich 2001), the uncorrelated noise in the radial wind velocity was estimated to be less than $0.15\,\mathrm{m\,s^{-1}}$ for SNR better than −8 dB (6 MHz bandwidth, accumulating 500 pulses). Using data collected during the scanning mode, a velocity azimuth display (VAD) technique (Browning and Wexler 1968) was applied to calculate a profile of mean horizontal wind speed and direction. Data sampled during the vertical stare mode provide high-resolution measurements of the vertical wind speed.

Table 4 Overview of measurement days

Date	Local cloud conditions	VAD	w_L (mm s^{-1})
22 June 2005	Full-day cloud-free conditions, around 1400 UTC structures in the backscatter signal which indicate thin clouds	None	-1.7 ± 7.2
27 June 2005	Full-day cloud-free conditions	None	1.1 ± 9.8
10 July 2005	Full-day cloud-free conditions	None	12.3 ± 10.0
11 July 2005	Small cumulus humilis	None	1.9 ± 6.2
14 July 2007	Full-day cloud-free conditions	30 min	-8.7 ± 12.3
15 July 2007	Full-day cloud-free conditions	30 min	-8.3 ± 17.7
01 August 2007	Full-day cloud-free conditions	30 min	-10.0 ± 15.5
05 August 2007	Full-day cloud-free conditions	30 min	-19.4 ± 24.1
31 July 2008	Cloud-free until 1300 UTC, afterwards small cumulus humilis	60 min	10.1 ± 15.7
06 August 2008	Full-day cloud-free conditions	60 min	0.1 ± 12.0
17 August 2008	Cloud-free until 1600 UTC, afterwards stratocumulus clouds	60 min	3.6 ± 10.5
27 August 2008	Full-day cloud-free conditions	60 min	-2.5 ± 10.2

VAD column displays the time interval at which a vertical profile of the horizontal wind is estimated from lidar data. (The temporal availability of vertical profiles of the horizontal wind from the lidar data depends on the scan strategy.) The large scale subsidence, w_L, was estimated from Global Forecast System model output at 700 hPa at 1200 UTC

To obtain a suitable dataset, measurements from three field campaigns are used: the Convective Storm Initiation Project (CSIP, Browning et al. 2007) conducted in 2005 in southern England; the Convective and Orographically-induced Precipitation Study (COPS, Wulfmeyer et al. 2008; Kottmeier et al. 2008) undertaken in 2007 in South Germany and France, and the Convective Boundary Layers with Doppler Lidar (CoBoLd) study performed in 2008 at the Karlsruhe Institute of Technology (KIT), Germany. The field campaigns differ relating to the terrain: the lidar was located in inhomogeneous terrain with flat vegetation during CSIP, in complex terrain at the highest peak of the Hornisgrinde mountain (1,165 m above sea level) during COPS, and in flat terrain with inhomogeneous vegetation during CoBoLd.

During CSIP and COPS, an energy balance station was placed near the lidar. The horizontal wind speed and direction, the potential temperature, the turbulent heat flux, and momentum fluxes were measured around 3 m above ground level and evaluated according to Kalthoff et al. (2006). During CoBoLd, equivalent measurements with the KIT 200-m tower (Barthlott et al. 2003) were conducted 40 m above the ground, which was the lowest measurement height above the treetops.

From each campaign, four cloudfree summer days were selected to ensure mostly convectively driven turbulence; Table 4 provides an overview of the measurements. Local cloud conditions were observed using a cloud camera placed on the top of the lidar container. The large-scale subsidence, w_L, was estimated using Global Forecast System model data (see Sect. 3.2 for details). On the first seven measurement days in Table 4 radiosondes were launched at the lidar site, for the other days operational radiosondes from the nearest station to the lidar were used (CSIP—Herstmonceux, COPS—Stuttgart, CoBoLd—Stuttgart).

3.2 Data Processing

Boundary-layer height: determining boundary-layer height is a well-known meteorological problem. Although it is of fundamental importance, estimates differ depending on the meteorological parameter, the measurement instrument, and even on the algorithm used (Seibert et al. 2000). In this study, two lidar-based parameters were used: on the one hand, the aerosol backscatter I_b, which results in an estimate of an aerosol-layer height, h_aero, on the other hand the vertical velocity variance, σ_w^2, which was taken to estimate a turbulence height, h_turb. Four automated methods, adopted from the literature, were used to determine h_aero: (i) using a threshold value (Melfi et al. 1985; Batchvarova et al. 1999); (ii) determining the minima of the height gradient $\partial I_\mathrm{b}/\partial z$ (Flamant et al. 1997; Lammert and Bösenberg 2006); (iii) fitting an idealized aerosol backscatter profile to the measured profile (Steyn et al. 1999; Haegeli et al. 2000), and (iv) using a wavelet analysis (Cohn and Angevine 2000; Davis et al. 2000; Brooks 2003). The different methods were evaluated against each other and show mostly consistent results. Method (iii) was found to display the boundary-layer height evolution with the most details and, therefore, h_aero derived using this method was chosen if at least one of the other three methods determined h to $\pm 100\,\mathrm{m}$ of this value. The value of h_aero is determined with a time resolution of 0.1 Hz.

The second parameter used to estimate h is the vertical wind velocity variance, which can be interpreted as a measure of turbulent kinetic energy and, therefore, as a direct measure of turbulence. Three methods were used to determine h_turb, all based on the widely accepted idealized profile of Lenschow et al. (1980):

$$\frac{\sigma_\mathrm{w}^2}{w_*^2} = 1.8\left(\frac{z}{h}\right)^{\frac{2}{3}}\left(1-0.8\frac{z}{h}\right)^2. \tag{10}$$

These are (i) the relationship between the height level of $\sigma_\mathrm{w,max}^2$ and h (Asimakopoulos et al. 2004); (ii) a threshold value ($\sigma_{w,\mathrm{threshold}}^2 = 0.16\,\mathrm{m^2\,s^{-2}}$) (Tucker et al. 2009), and (iii) a fit of an idealized profile of σ_w^2 to the measured profile. The vertical velocity variance was estimated based on data obtained during time intervals of 60 min. The variances were corrected for uncorrelated noise using the difference between lag one and lag zero of the autocorrelation function (Lenschow et al. 2000a). Method (i) was found to differ in many situations from methods (ii) and (iii). One reason might be that the maximum of Eq. 10 is in the lowest one-third of the convective boundary layer and the minimum measurement height of the lidar is about 350 m above the ground. This might also cause fitting problems for small values of the boundary-layer height using method (iii). Thus, the results from method (ii) were chosen to represent h_turb, which is also closest to the definition of the boundary layer.

Figure 1 shows a comparison between h_aero and h_turb. Although the correlation coefficient $R = 0.82$ seems large, it is obvious that the two parameters yield contrasting concepts of boundary-layer height: whereas the turbulence height displays the current extent of the turbulent zone, the aerosol-layer height is a record of the history of turbulence. This becomes apparent especially during the afternoon transition to a residual layer. To ensure that there exists at least weak turbulence, only aerosol-layer heights with $\sigma_\mathrm{w}^2(h_\mathrm{aero}) \geq 0.04\,\mathrm{m^2\,s^{-2}}$ were used for further investigation.

Entrainment velocity: the daily evolutions of h_aero and h_turb were smoothed with cubic splines, and the growth rate dh/dt was estimated by linear regression. According to Eq. 1, the large-scale subsidence, w_L, is needed to estimate the entrainment velocity. To determine w_L empirically a network of meteorological stations can be used, e.g. Boers et al. (1984) and Nelson et al. (1989), though such networks were not installed during the measurement

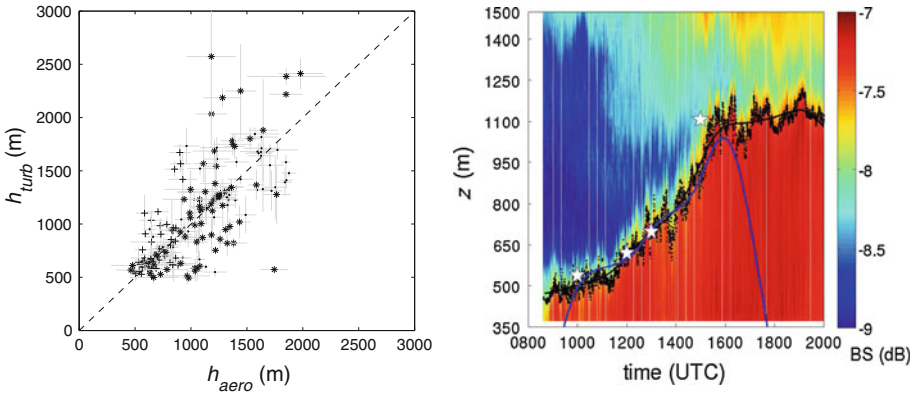

Fig. 1 *Left* Turbulence height (based on 60-min time intervals) as a function of 60-min-averaged values of the aerosol-layer height. The different *symbols* indicate the three measurement campaigns: *dots* CSIP, *plus* COPS, and *stars* CoBoLd. h_{aero} *error bars* represent standard deviations during the considered time intervals, h_{turb} *error bars* show the variation using time intervals for estimating h_{turb} shifted by 1 min. *Right* Aerosol backscatter and aerosol-layer height (*black line*) as well as turbulence height (*blue line*) on 27 June 2005. The *colours* represent the aerosol backscatter values. *White stars* indicating boundary-layer heights estimated from radiosonde profiles using the method of Driedonks (1982)

campaigns. Beyrich and Gryning (1998) and Yi et al. (2001) used height changes of significant structures in the aerosol backscatter data, but such structures were also not obvious in the lidar data of the considered days. To have at least an expectation, Global Forecast System model data were used for a rough estimation of vertical velocity at 700 hPa (Table 4). An averaged value of the model point at the measurement location and its nearest neighbours at 1200 UTC was calculated. The estimated w_{L}s show standard deviations of more than 100% of the mean value. Because of the rough w_{L} estimation from the Global Forecast System model, in the following a constant $w_{\mathrm{L}} = 0$ was assumed for all days, a value that is in the error range of the Global Forecast System w_{L} model output. If the real large-scale subsidence is $w_{\mathrm{L}} = -10\,\mathrm{mm\,s^{-1}}$ (and not $w_{\mathrm{L}} = 0$ as assumed in this study) and the boundary-layer growth rate is assumed to be $\mathrm{d}h/\mathrm{d}t = 15\,\mathrm{mm\,s^{-1}}$ ($50\,\mathrm{mm\,s^{-1}}$), a relative error in w_{e} of 0.4 (0.17) occurs. So especially for small boundary-layer height growth rates, the assumption of a constant $w_{\mathrm{L}} = 0$ is a limitation in this study.

Entrainment-zone thickness: similar to the lack of a robust boundary-layer height definition, the entrainment-zone thickness is estimated in various ways in the literature. It is possible to distinguish between statistically-based definitions on the one hand, using percentiles or the standard deviation of $h(t)$, or $h(\mathbf{x})$ respectively, (e.g. Melfi et al. 1985; Davis et al. 1997; Cohn and Angevine 2000), and a transition-zone definition on the other hand, using the transition of temperature, moisture or aerosol from a boundary-layer value to a free atmosphere value (e.g. Haegeli et al. 2000). In this study, both concepts were considered.

Because of the high time resolution, h_{aero} offers the possibility of estimating the statistical entrainment-zone thickness. Here, the difference between the 4th (h_0) and the 98th (h_2) percentile of the trend-corrected aerosol-layer height in a 60-min time interval is used. For other statistical measures (difference between the 15th and the 85th percentile or the standard deviation of h_{aero}) correlation coefficients $R > 0.96$ were found. A transition zone, Δh_{TZ}, between a high aerosol content in the boundary layer to a low value in the free atmosphere is a fit parameter in method (iii) for determining the aerosol-layer height (see paragraph 1, this section).

A correlation coefficient between $h_2 - h_0$ and Δh_{TZ} of 0.25 indicates that the concepts differ significantly. One reason might be that the statistically-based concept, linked to a set of boundary-layer height estimations, captures temporal, spatial and small-scale turbulence variations, whereas the transition-zone concept, linked to single profiles, displays only the small-scale turbulence.

Integral length scale: this length scale is that below which the vertical wind velocity is significantly correlated with itself (Lenschow and Stankov 1986), and can be interpreted as the size of the dominant eddies (Lothon et al. 2009). In the turbulent boundary layer, the autocorrelation function of the vertical wind velocity shows approximate exponential decay (Lothon et al. 2006), which was used to determine an integral time scale using a least-squares fit. The exponential fit was made on the zero-lag corrected autocorrelation function (Lenschow et al. 2000a), based on 60-min time intervals. Using Taylor's hypothesis of frozen turbulence, the integral time scale is then converted into an integral length scale. It was found that l varies little over the boundary layer, so that averaging is reasonable.

Velocity scales: convective velocity is estimated using the surface-flux measurements and the smoothed values of h_{aero} and h_{turb}. $\sigma_{\text{w,max}}$ in the convective boundary layer is calculated using the noise-corrected profile of vertical velocity variance for time intervals of 60 min.

Richardson number: because the temperature jump across the entrainment zone could not be reliably determined with the available instrument set-up, a modified Richardson number, $\tilde{Ri}$, suggested by Deardorff (1979) is used:

$$\tilde{Ri}(L, V) = g \frac{\gamma}{\overline{\theta}} \frac{L^2}{V^2}, \tag{11}$$

where γ is the temperature gradient in the free atmosphere and $\overline{\theta}$ is the mean boundary-layer potential temperature. Both γ and $\overline{\theta}$ were estimated from radiosonde profiles visually. $\tilde{Ri}$ gives greater weighting to the length scale compared to Ri. Figures 4 and 5 show the relationships between entrainment parameters and $\tilde{Ri}$ based on data obtained by Deardorff et al. (1980) and Boers and Eloranta (1986). It is obvious that the modified Richardson number has the same potential to be used in parametrizations as does Ri.

4 Results

4.1 Entrainment Regimes

The lidar observations show the following structures at the interface between the convective boundary layer and the free atmosphere:

(i) In several situations, bulging of the aerosol-laden layer with strong underlying updrafts was observed. Here, the deformation of the convective boundary layer and the wind structure are assumed to be related. Entrainment is expected during the recoil processes (Linden 1973) or at the edges of the deformation region (Sullivan et al. 1998). The latter could be observed as downward movements as shown in Fig. 2, left.

(ii) The interface shows wavelike structures of different wavelengths (from several tens of metres up to kilometres) and amplitudes, which were probably caused by shear instabilities. It was possible to observe structures, which even show a tendency to breakdown as shown in Fig. 2, middle.

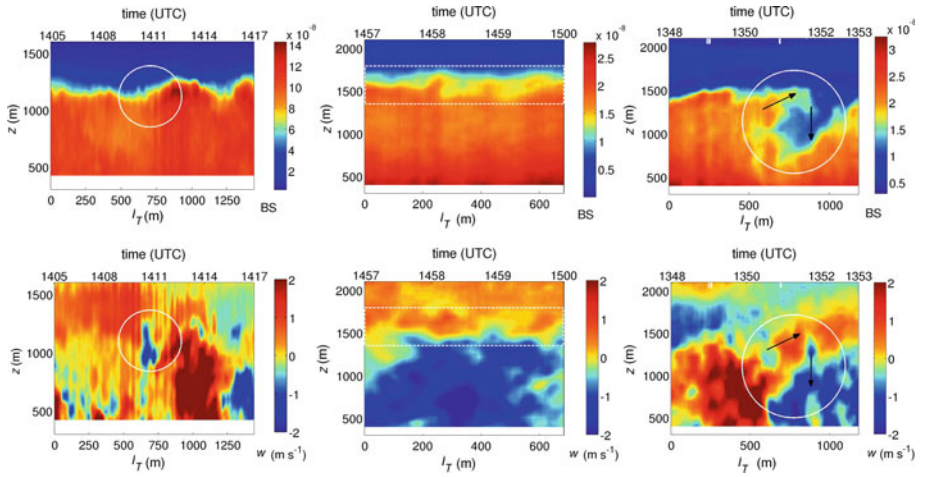

Fig. 2 Entrainment events between the convective boundary layer and the free atmosphere for varying stability in the free atmosphere. The *upper pictures* show the uncalibrated aerosol backscatter, *warm colours* representing high aerosol load; the *lower pictures* show the vertical wind velocity. The top of the aerosol layer is clearly visible by the changing *colours* from *red* to *blue* in the *upper pictures*. From *left to right*: deformation of the interface due to impinging plumes, wavelike structures (potentially from shear instabilities), and large-scale engulfment

(iii) Several situations show an engulfment of aerosol-depleted air by aerosol-laden air. It is possible to visualize the enclosing process with the typical wind field (Fig. 2, right) as well as enclosed areas of air with a low aerosol content in the aerosol-laden layer.
(iv) A few situations show a rip-off of the interface. Regions of the aerosol-laden air can be found in the free atmosphere.

However, entrainment due to the generation and breaking of internal waves, which was introduced in Sect. 2.1, was not observed. Note that the frames in Fig. 2 show single situations, which cover short time periods. Vertical velocities, i.e. updrafts and downdrafts, in the boundary layer, as well as vertical motions in the free atmosphere, are not representative for longer time periods. In the left and right frames the vertical velocity in the aerosol-laden layer can be directly related to the shown process. In the middle frame, the vertical velocity seems to be not linked, although the strong gradient in vertical velocity might give a hint to the existence of shear.

Using the above identified processes, the entrainment zones of nine measurement days (Table 5), during the period from 1030 to 1330 UTC, were related subjectively to one of three entrainment-zone classes: class 1 is characterized by a well-defined passage from the aerosol-laden layer to the aerosol-depleted layer with high gradients $-\partial I_\mathrm{b}/\partial z$. Weak wave motions with wavelengths of several hundred to 1,000 m and low amplitude were observed. These interfaces respond well to impinging turbulence elements. Showing no engulfment or rip-off, entrainment is dominated by process (i). Class 2 has an interface with high variability and considerable wave-like motions, but no deep engulfment or rip-off. Bulging of the interface could often not be related to the vertical wind beneath. Mechanism (ii) is the dominant entrainment process. A strongly disturbed interface, showing large-scale engulfment and rip-off, is classified as class 3. Here it is sometimes not possible to discriminate between the mixed layer and the entrainment zone.

Table 5 Entrainment-zone classes and averaged boundary-layer parameters

Date	Class	γ (K m^{-1})	$\overline{w'\theta'}_0$ (K m s^{-1})	$\tilde{Ri}(h, w_*)$	$\tilde{Ri}(l, \sigma_{w,max})$
22 June 2005	2	3.5×10^{-3}	0.11 ± 0.02	47 ± 17	1.9 ± 0.8
27 June 2005	1	8×10^{-3}	0.18 ± 0.05	46 ± 14	2.8 ± 1.0
10 July 2005	3	$<1 \times 10^{-3}$	0.16 ± 0.03	9 ± 10	1.1 ± 1.2
01 August 2007	2	7×10^{-3}	0.20 ± 0.03	36 ± 9	5.5 ± 4.4
05 August 2007	2	6×10^{-3}	0.20 ± 0.02	26 ± 8	12.7 ± 8.0
31 July 2008	3	1×10^{-3}	0.39 ± 0.12	7 ± 7	0.5 ± 0.5
06 August 2008	2	5×10^{-3}	0.21 ± 0.09	67 ± 31	3.4 ± 2.2
17 August 2008	1–2	1×10^{-3} [a]	0.22 ± 0.04	91 ± 22	2.5 ± 1.2
27 August 2008	1	7×10^{-3}	0.22 ± 0.05	72 ± 20	4.7 ± 2.3

For 14 July 2007 and 15 July 2007 the top of the aerosol layer was less clearly defined due to advection processes and mesoscale effects (Kalthoff et al. 2009), for 11 July 2005 the top was affected by clouds. All these effects complicate the identification of individual processes

[a] Second stable layer 750 m above with $\gamma = 8 \times 10^{-3}$ K m^{-1}

Setting the assigned entrainment-zone class in conjunction with averaged turbulence and stability parameters (temperature gradient in the free atmosphere, turbulent temperature flux at the ground and modified Richardson number, Table 5), a relation between the class and γ was found. At high stability ($\gamma = 0.007$–0.008 K m^{-1}), entrainment zones of class 1 can be observed, followed by class 2 entrainment zones at $\gamma = 0.003$–0.007 K m^{-1}. Class 3 entrainment zones finally have a vertical temperature gradient $\gamma \leq 0.001$ K m^{-1}. $\overline{w'\theta'}_0$ varies too little to show a correlation with the identified entrainment-zone classes. Whereas in previous studies (Sect. 2) the occurrence of different entrainment processes was linked to different Richardson numbers, this could not be confirmed here, with the exception that class 3 interfaces are characterized by outstanding small values of $\tilde{Ri}$.

The mean entrainment velocity and the mean entrainment-zone thickness from 1030 UTC to 1330 UTC as a function of γ are presented in Fig. 3. Both conceptual approaches for boundary-layer height (aerosol layer and turbulence heights) as well as both approaches for entrainment-zone thickness (statistical and transition-zone concepts) are shown. Especially for the entrainment velocities based on the aerosol-layer height and the statistical entrainment-zone thickness a high anticorrelation with γ ($R = -0.93$, and -0.77 respectively) occurs. The other measures, h_{turb} and Δh_{TZ}, at least show an equivalent tendency of decreasing w_e and Δh with increasing stability. Table 5 indicates that γ is linked to different entrainment processes, which now, in turn, seem to lead to different entrainment-zone thicknesses and have a different entrainment efficiency, i.e. are able to entrain different amounts of free atmosphere air, which leads to different entrainment velocities.

In summary, it is possible to distinguish between different entrainment regimes. Due to different dominating entrainment processes, these regimes show different entrainment-zone thicknesses as well as entrainment velocities. The regimes appear to depend on the stability of the free atmosphere. Concerning the robustness of this outcome, it has to be considered that only nine datasets are available and therefore more testing is needed.

4.2 Entrainment-Zone Thickness and Entrainment Velocity Parametrizations

All parametrizations introduced in Sect. 2.3, i.e. "Constant-ratio-parametrizations", "Simple-stability-parametrizations", "Direct-relationship-parametrizations" as well as

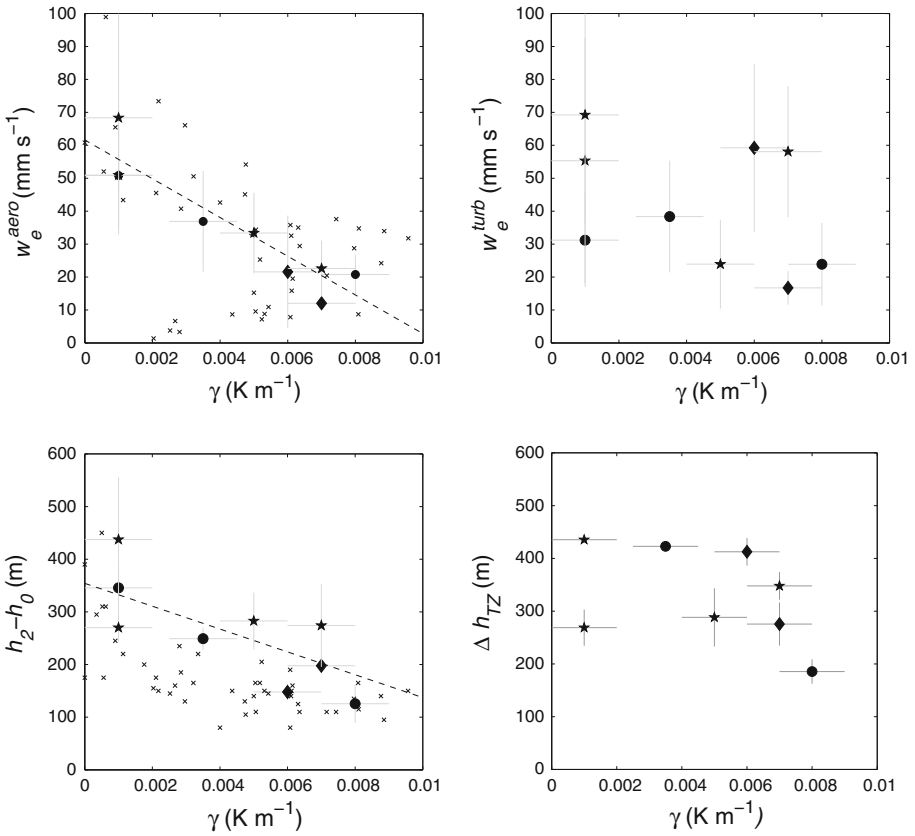

Fig. 3 Entrainment velocity (*above*) and entrainment-zone thickness (*below*) as a function of the potential temperature gradient in the free atmosphere. w_e^{aero} represents the entrainment velocity based on aerosol-layer heights, w_e^{turb} the entrainment velocity based on turbulence heights. $h_2 - h_0$ is based on the statistical entrainment-zone thickness concept, Δh_{TZ} is based on the transition-zone concept. The *bold symbols* mark the three campaigns, i.e. *dots* CSIP, *diamonds* COPS, and *stars* CoBoLd. *Error bars* are the standard deviation of w_e, and Δh respectively, during 1030 and 1330 UTC, for γ a constant error of 0.001 K m^{-1} was used. The *small crosses* represent data obtained by Boers and Eloranta (1986)

"Extensive-stability-parametrizations", were reviewed using the two-scale combinations (h, w_*) and $(l, \sigma_{w,max})$. Here, it is of interest whether the quality of the relationship changes when the scale combination is changed. Table 6 shows an overview of all concepts and results. To ensure consistency h_{aero} was used as the length scale in association with w_e^{aero} as well as h_{turb} in association with w_e^{turb}. The columns four and five show the correlation coefficients between parameters one and two using conventional scales (column 4), and turbulent scales (column 5) respectively. Further explanation is given in the following paragraphs.

(i) "Constant-ratio-parametrizations" were tested using all 12 cases (Table 4), from 0800 to 1800 UTC. It is remarkable that here, the turbulence height concept yields higher correlation coefficients than the aerosol-layer height concept (Table 6). This might be explained by considering aerosol-layer heights from the later afternoon, when turbulence-layer heights are not longer determinable because of too weak turbulence. During this time period the entrainment zone no longer exists according to its originally meaning. The small-scale

Table 6 Correlation coefficients for different types of entrainment parametrizations

	Parameter 1	Parameter 2	Conventional scales		Turbulent scales	
			h^{aero}, h^{turb}	w_*	l	σ_{w}
"Constant-ratio-parametrizations"	$h_2 - h_0$	L	0.44, 0.57		0.3	
	Δh_{TZ}	L	<0.1		<0.1	
	$w_{\mathrm{e}}^{\mathrm{aero}}$, $w_{\mathrm{e}}^{\mathrm{turb}}$	V		0.37, 0.06		0.26, −0.20
"Simple-stability-parametrizations"	$h_2 - h_0$	$\tilde{Ri}^{-0.5\,\mathrm{a}}$	0.46		0.85	
	Δh_{TZ}	$\tilde{Ri}^{-0.5\,\mathrm{a}}$	−0.36		0.12	
	$w_{\mathrm{e}}^{\mathrm{aero}}$, $w_{\mathrm{e}}^{\mathrm{turb}}$	$\tilde{Ri}^{-0.5}$	0.31, 0.16		0.56, 0.21	
"Direct-relationship-parametrizations"	$h_2 - h_0$	$w_{\mathrm{e}}^{\mathrm{aero}}$	0.60		0.45	
	$h_2 - h_0$	$w_{\mathrm{e}}^{\mathrm{turb}}$	0.17		0.11	
	Δh_{TZ}	$w_{\mathrm{e}}^{\mathrm{aero}}$	0.37		0.46	
	Δh_{TZ}	$w_{\mathrm{e}}^{\mathrm{turb}}$	0.43		0.51	
"Extensive-stability-parametrizations"	$h_2 - h_0$	$\tilde{Ri}_{w_{\mathrm{e}}}^{-1/3\,\mathrm{a}}$	0.41		0.81	
	Δh_{TZ}	$\tilde{Ri}_{w_{\mathrm{e}}}^{-1/3\,\mathrm{a}}$	−0.21		0.36	

See the text for more details

[a] For the aerosol-layer height concept, the turbulence height concept yields similar results

transition-zone concept does not correlate with the large-scale boundary-layer, height for both boundary-layer height concepts ($R < 0.1$).

For both length scales, $L = h$ as well as $L = l$, and both entrainment-zone thickness measures, the ratio $\Delta h/L$ shows a frequency distribution that is log-normal. Expected values are in the order of 0.2 to 0.3 for $L = h$ and 1.5 to 2.0 for $L = l$, which is in agreement with values found in previous studies (e.g. Crapper and Linden 1974; Deardorff 1983). During the COPS campaign at the measurement site on top of a mountain, the ratio $\Delta h/h$ was considerably larger than during the two other campaigns—an effect that is directly related to smaller boundary-layer heights over the mountain peak, and not due to a change in the Δh distribution. This effect is not recognisable in the ratio $\Delta h/l$. A systematically changing behaviour of $\Delta h/L$ dependent on the time of day was not found.

For both boundary-layer height concepts, w_{e} showed correlation coefficients $|R| < 0.37$ for both velocity scales w_* and $\sigma_{\mathrm{w,max}}$.

(ii) "Simple-stability-parametrizations" were examined using the three cloud-free days in 2005, 1 and 5 August 2007 and the four days in 2008, always for the period 1030 UTC to 1330 UTC. Figures 4 and 5 show the results for both boundary-layer height concepts and, therefore, entrainment velocity, and the statistical entrainment-zone thickness concept. A systematically different behaviour of the two boundary-layer height concepts is not obvious, mainly because only data in the high turbulence period are used.

For entrainment velocity (Fig. 4), a small exponent β in Eq. 6 between 0.25 and 0.5 is evident, which is in contradiction to the values found in previous studies (Table 2). Extending the data by using the results obtained by Deardorff et al. (1980) and Boers and Eloranta (1986) increases the exponent. A linear relationship between w_{e}/V and $\tilde{Ri}^{-0.5}$ showed an increase in the correlation coefficient from 0.31 to 0.56 when the turbulent scales are used instead of the conventional scales. A least-squares fit using $\beta = 0.5$ yields numerical values of

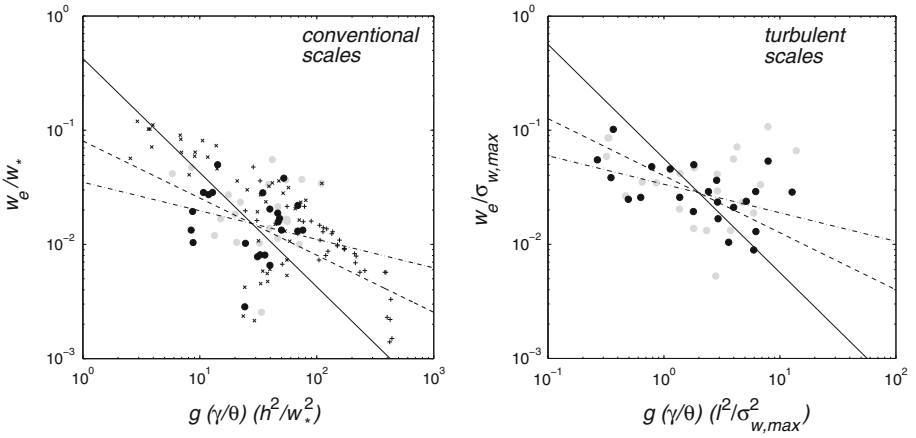

Fig. 4 Relationships between the normalized entrainment velocity and the modified Richardson number: conventional scales (h, w_*) on the *left*, and new turbulent scales (l, $\sigma_{\mathrm{w,max}}$) on the *right panel*. *Black dots* denote the aerosol-layer height estimate, *grey dots* the turbulence height estimate. *Pluses* represent data obtained by Deardorff et al. (1980), *crosses* data obtained by Boers and Eloranta (1986). For a better guidance, best fits for exponent $\beta = 1$ (*black solid line*), $\beta = 0.5$ (*black dashed line*) and $\beta = 0.25$ (*black dot-dashed line*) are also included

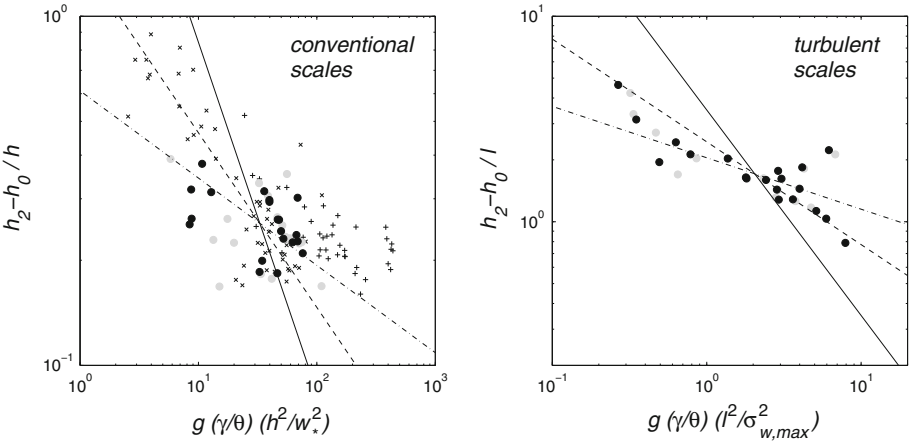

Fig. 5 Relationships between the normalized entrainment-zone thickness and the modified Richardson number: conventional convective boundary-layer scales (h, w_*) were used in the *left frame*, and new turbulent scales (l, $\sigma_{\mathrm{w,max}}$) in the *right frame*. *Symbols* correspond to those used in Fig. 4

$$\frac{w_{\mathrm{e}}}{\sigma_{\mathrm{w,max}}} = (23.7 \pm 16.4)\ 10^{-3}\ \tilde{Ri}^{-0.5} + (13.6 \pm 15.6)\ 10^{-3}. \tag{12}$$

Figure 5 shows the effect of changing scales in the relationship between the normalized entrainment-zone thickness and $\tilde{Ri}$ using the statistical entrainment-zone thickness concept. Considerably less scatter and a clearer functional relation are obvious when the turbulent scales are used instead of the conventional ones. Exponent b in Eq. 5 could be estimated between 0.25 and 0.5, which is considerably less than 1 and in agreement with the studies of Boers (1989); Gryning and Batchvarova (1994) and Fedorovich et al. (2004) (Table 1).

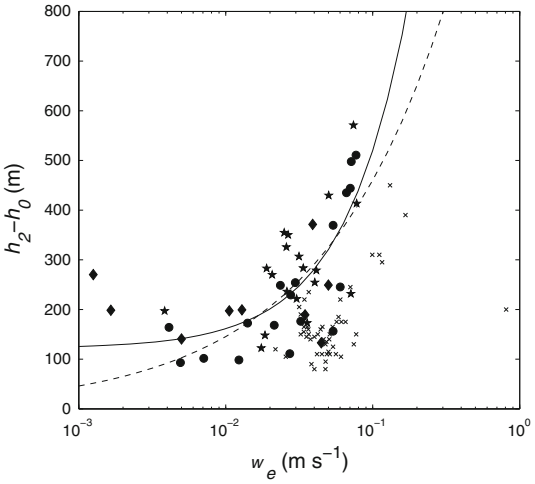

Fig. 6 Relationship between the entrainment-zone thickness (statistical concept) and the entrainment velocity based on the aerosol-layer height. The *bold symbols mark* the three campaigns, i.e. *dots* CSIP, *diamonds* COPS, and *stars* CoBoLd. The *small crosses* are data taken from Boers and Eloranta (1986), the *solid line* is the least-squares fit with finite threshold of the entrainment-zone thickness if $w_e \to 0$ and $m = 1$, the *dashed line* is the least-squares fit with zero threshold of the entrainment-zone thickness if $w_e \to 0$ and $m = 0.5$

Using $b = 0.5$, an increase in the correlation coefficient from 0.46 to 0.85 results when the scales are changed from (h, w_*) to $(l, \sigma_{w,\max})$. Least-squares fits yield numerical values of

$$\frac{h_2 - h_0}{h} = (0.29 \pm 0.26)\,\tilde{Ri}^{-0.5} + (0.21 \pm 0.05), \tag{13}$$

and

$$\frac{h_2 - h_0}{l} = (1.60 \pm 0.50)\,\tilde{Ri}^{-0.5} + (0.58 \pm 0.43). \tag{14}$$

Both parametrizations show a threshold value for high stability, and the widely used numerical value of $\lim_{\tilde{Ri}\to\infty}(h_2 - h_0)/h = 0.2$ (going back to Deardorff et al. 1980) is confirmed.

The transition-zone concept shows small correlation coefficients, which were determined by outliers related to days with the type entrainment-zone class 3 (Sect. 4.1).

To investigate class (iii) "Direct-relationship-parametrizations", the whole dataset (Table 4) from 0800 to 1800 UTC was used. The correlation coefficients in Table 6 were calculated using only the two campaigns CSIP and CoBoLd. First, the dependency between the entrainment-zone thickness and the entrainment velocity was investigated using unity scales $L = 1\,\mathrm{m}$ and $V = 1\,\mathrm{m\,s^{-1}}$, i.e. no scaling. Figure 6 shows the results for the aerosol-layer height concept and the statistical entrainment-zone thickness. A connection between broader Δh and higher w_e is clearly evident, while the COPS dataset shows no deviant behaviour. The best value of the exponent m in Eq. 7 depends on specifications of the threshold $\lim_{w_e\to 0}(h_2 - h_0) = c$. If $c = 0$, a least-squares fit using $m = 0.5$ shows a higher quality compared to $m = 1$, otherwise, when a finite threshold is assumed, the fit using $m = 1$ adjusts better to the data.

Using conventional scales for normalization an analogous effect was found. Figure 7, left, shows the result for the statistical entrainment-zone thickness concept and the aerosol-layer height. Here, the COPS campaign shows anomalous behaviour with higher $\Delta h/h$ because of smaller boundary-layer heights over the mountain top. The results from CSIP and CoBoLd campaigns fit nicely into the results from previous studies. Using $\lim_{w_e/w_*\to 0}(h_2 - h_0)/h = 0$, a least-squares fit gives an exponent $m = 0.29 \pm 0.14$. In this case, the quality of the fit is higher if $m = 0.5$ is used instead of $m = 1$. Otherwise, using a finite threshold $c > 0$, $m = 1$ yields a better fit than $m = 0.5$. The numerical values

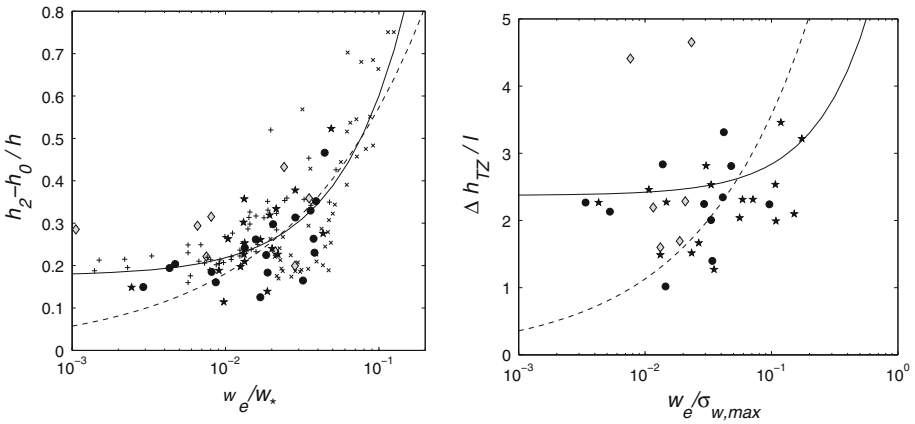

Fig. 7 Relationship between the normalized entrainment-zone thickness and the entrainment velocity using the conventional scales and the aerosol-layer height concept (*left*), and between the normalized entrainment-zone thickness and the entrainment velocity using the turbulent scales and the turbulence height concept (*right*). *Symbols* correspond to those used in Fig. 6, results obtained by Deardorff et al. (1980) (*plus*) are included in addition

$$\frac{h_2 - h_0}{h} = (4.8 \pm 1.9)\left(\frac{w_e}{w_*}\right)^1 + (0.16 \pm 0.05), \tag{15}$$

and

$$\frac{h_2 - h_0}{h} = (1.8 \pm 0.2)\left(\frac{w_e}{w_*}\right)^{0.5} \tag{16}$$

agree with values found in previous studies (Table 3). The different applications of a threshold value for $\lim_{w_e/V \to 0} \Delta h/L$ in previous studies may therefore be one reason for the different exponents found.

Going from conventional scales to turbulent scales, no continuous improvement in this relationship was observed (Fig. 7; Table 6). The highest correlation coefficient was found for the combination of aerosol-layer height and statistical entrainment-zone thickness using conventional scales. This combination of parameters seems to have the highest capability to describe the convective boundary-layer growth, and combines all concepts to date that are mostly used in parametrizations.

(iv) An "Extensive-stability-parametrization" was tested using data as in paragraph (ii) in this section. Figure 8 shows the result using the two scale combinations and the statistical entrainment-zone thickness concept.

Again, it is obvious that the data show a clearer relationship with less scatter when the turbulent scales are used. The correlation coefficient between $(h_2 - h_0)/L$ and $\tilde{Ri}_{we}^{-1/3}$ increases from 0.41 to 0.81 by changing $L = h$ to $L = l$. A least-squares fit results in

$$\frac{h_2 - h_0}{h} = (2.27 \pm 2.61)\tilde{Ri}_{we}^{-1/3} + (0.21 \pm 0.06), \tag{17}$$

and

$$\frac{h_2 - h_0}{l} = (15.16 \pm 4.59)\tilde{Ri}_{we}^{-1/3} + (0.59 \pm 0.48). \tag{18}$$

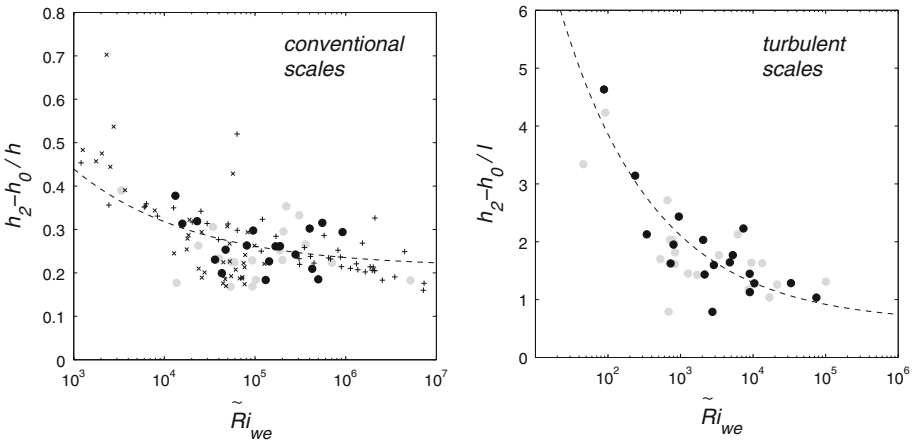

Fig. 8 Relationships between the normalized entrainment-zone thickness and the modified Richardson number using entrainment velocity: conventional convective boundary-layer scales (h, w_*) in the *left*, and new turbulent scales (l, $\sigma_{w,max}$) in the *right picture*. *Black dots* using the aerosol-height concept, *grey dots* the turbulence height concept, *pluses* data obtained by Deardorff et al. (1980), *crosses* represent data obtained by Boers and Eloranta (1986). The *black dashed line* is a best fit through the data

The transition-zone concept yields lower correlation coefficients for all boundary-layer height concepts.

5 Conclusions

The entrainment of air from the free atmosphere into the turbulent convective boundary layer is a problem that has been considered in theoretical models, laboratory studies, field campaigns and numerical studies for many years. Here we investigate such entrainment with Doppler lidar wind and aerosol data, which allow good visualization of the entrainment process and simultaneously a characterization of the turbulence throughout the whole boundary layer. Different concepts of entrainment-zone thickness (statistical and transition-zone concepts) and boundary-layer height (aerosol layer and turbulence heights) and different scales, especially for differentiation between scales used conventionally in atmospheric boundary-layer research (h and w_*) and fluid mechanics (l and $\sigma_{w,max}$), are considered and compared.

Different conceivable fluid entrainment processes are identified: the deformation of the interface due to impinging eddies and plumes; the generation of waves at the interface, which show breaking patterns; and the engulfment of aerosol-depleted air by aerosol-laden air. Based on the different processes, entrainment-zone classes were defined, which can be linked to atmospheric situations, which differ depending on the stability of the free atmosphere. An equivalent behaviour can be seen for Δh and w_e. In summary different entrainment regimes are discernable, although these results need further testing.

Concerning the entrainment parametrization, four different complex classes of relationships were examined. In general it turns out that the concepts of statistical entrainment-zone thickness and aerosol-layer height, which were used so far in entrainment parametrizations, showed the clearest relationships with least scatter. Although the concept of turbulence height should be able to display the current extent of the turbulent zone more reliably compared to the aerosol-layer height, it showed partly lower correlation coefficients. Additionally, it has

the disadvantage of a low temporal resolution when obtained from ground-based lidar. The transition-zone concept for entrainment-zone thickness shows low correlation coefficients in all parametrization classes. It might be reasonable to reject this as an entrainment-zone concept, which can be obtained from lidar measurements.

The simplest entrainment parametrization used a direct proportionality between the entrainment-zone thickness and a length scale, and the entrainment velocity and a velocity scale. $\Delta h/L$, and w_e/V respectively, are distributed log-normal with expected values in the order of previously found results. Also numerical values found in previous studies for a relationship between the normalized entrainment-zone thickness and the normalized entrainment velocity, without explicitly considering stability, were confirmed. Here, the correlation coefficients showed no considerable change, when changing the scales from (h, w_*) to $(l, \sigma_{w,max})$. Parametrizations including stability were tested using a modified Richardson number, and these types of parametrizations yield the highest correlation coefficients. A change in the scales from (h, w_*) to $(l, \sigma_{w,max})$ increases the correlation coefficient by a factor of up to 2.

For several parameter configurations the turbulent scales yield improved relationships. One reason for this result might be that l and $\sigma_{w,max}$ are more closely connected to the driving processes of entrainment, i.e. the turbulent eddies, than (h, w_*). Whereas boundary-layer height is just an indicator or a record of the turbulence, the integral length scale represents the instantaneous size of the dominant eddies. The standard deviation of vertical velocity quantifies the velocity fluctuations, whereas the convective velocity is a derivative of the turbulent surface flux and the boundary-layer height. The turbulent scales are now directly available from lidar measurements and may therefore help to improve entrainment parametrizations. Although it has to be considered that these scales may be difficult to use in numerical models, because they are subgrid variables, and have to be parametrized themselves.

Acknowledgments The authors would like to thank Dr. Donald H. Lenschow for his encouragement in the topic and editorial hints in the manuscript and Dr. BenBella Shannak for his view from an engineer's perspective on the problem. Also thanks to Holger Mahlke for extracting the data from the GFS model. And thanks to the three anonymous reviewers, whose comments helped to improve the paper. The manuscript is based on results of a PhD thesis carried out with support of the Karlsruhe Institute of Technology (KIT).

References

Angevine W (2008) Transitional, entraining, cloudy, and coastal boundary layers. Acta Geophys 56(1):2–20

Angevine W, White A, Avery S (1994) Boundary-layer depth and entrainment zone characterization with a boundary-layer profiler. Boundary-Layer Meteorol 68:375–385

Asimakopoulos D, Helmis C, Michopoulos J (2004) Evaluation of sodar methods for the determination of the atmospheric boundary layer mixing height. Meteorol Atmos Phys 85:85–92

Baines W (1975) Entrainment by a plume or jet at a density interface. J Fluid Mech 68:309–320

Barthlott C, Kalthoff N, Fiedler F (2003) Influence of high-frequency radiation on turbulence measurements on a 200 m tower. Meteorol Z 12(2):67–71

Batchvarova E, Cai X, Gryning SE, Steyn D (1999) Modelling internal boundary-layer development in a region with a complex coastline. Boundary-Layer Meteorol 90:1–20

Beyrich F, Gryning SE (1998) Estimation of the entrainment zone depth in a shallow convective boundary layer from sodar data. J Appl Meteorol 37:255–268

Boers R (1989) A parameterization of the depth of the entraiment zone. J Appl Meteorol 28:107–111

Boers R, Eloranta E (1986) Lidar measurements of the atmospheric entrainment zone and the potential temperature jump across the top of the mixed layer. Boundary-Layer Meteorol 34:357–375

Boers R, Eloranta E, Coulter R (1984) Lidar observations of mixed layer dynamics: tests of parameterized entrainment models. J Clim Appl Meteorol 23:247–266

Brooks I (2003) Finding boundary layer top: application of a wavelet covariance transform to lidar backscatter profiles. J Atmos Ocean Technol 20:1092–1105

Browning K, Wexler R (1968) The determination of kinematic properties of a wind field using doppler radar. J Appl Meteorol 7:105–113

Browning K, Blyth A, Clark P, Corsmeier U, Morcrette C, Agnew J, Ballard S, Bamber D, Barthlott C, Bennett L, Beswick K, Bitter M, Bozier K, Brooks B, Collier C, Davies F, Deny B, Dixon M, Feuerle T, Forbes R, Gaffard C, Gray M, Hankers R, Hewison T, Kalthoff N, Khodayar S, Kohler M, Kottmeier C, Kraut S, Kunz M, Ladd D, Lean H, Lenfant J, Li Z, Marsham J, McGregor J, Mobbs S, Nicol J, Norton E, Parker D, Perry F, Ramatschi M, Ricketts H, Roberts N, Russell A, Schulz H, Slack E, Vaughan G, Waight J, Watson R, Webb A, Wareing D, Wieser A (2007) The convective storm initiation project. Bull Am Meteorol Soc 88(12):1939–1955

Calhoun R, Wieser A, Princevac M, Kottmeier C (2005) Comparison of lidar data with tower, profiler, radiosonde, and tethersonde data. In: European Geosciences Union General Assembly 2005, Vienna, Austria, 24–29 April 2005

Canut G, Lothon M, Said F, Lohou F (2010) Observation of entrainment at the interface between monsoon flow and the saharan air layer. Q J Roy Meteorol Soc 136:34–46

Carruthers D, Hunt J (1986) Velocity fluctuations near an interface between a turbulent region and a stably stratified layer. J Fluid Mech 165:475–501

Carruthers D, Moeng CH (1987) Waves in the overlying inversion of the convective boundary layer. J Atmos Sci 44(14):1801–1808

Caughey S, Palmer S (1979) Some aspects of turbulence structure through the depth of the convective boundary layer. Q J Roy Meteorol Soc 105:811–827

Cohn S, Angevine W (2000) Boundary layer height and entrainment zone thickness measured by lidars and wind-profiling radars. J Appl Meteorol 39:1233–1247

Conzemius R, Fedorovich E (2006) Dynamics of sheared convective boundary layer entrainment. Part I: methodological background and large-eddy simulations. J Atmos Sci 63:1151–1178

Couvreux F, Guichard F, Masson V, Redelsperger JL (2007) Negative water vapour skewness and dry tongues in the convective boundary layer: observations and large-eddy simulation budget analysis. Boundary-Layer Meteorol 123:269–294

Crapper P, Linden P (1974) The structure of turbulent density interfaces. J Fluid Mech 65(1):45–63

Davis K, Lenschow D, Oncley S, Kiemle C, Ehret G, Giez A, Mann J (1997) Role of entrainment in surface–atmosphere interactions over the boreal forest. J Geophys Res 102(D24):29219–29230

Davis K, Gamage N, Hagelberg C, Kiemle C, Lenschow D, Sullivan P (2000) An objective method for deriving atmospheric structure from airborne lidar observations. J Atmos Ocean Technol 17:1455–1468

Deardorff J (1970) Convective velocity and temperature scales for the unstable planetary boundary layer and for rayleigh convection. J Atmos Sci 27:1211–1213

Deardorff J (1979) Prediction of convective mixed-layer entrainment for realistic capping-inversion structure. J Atmos Sci 36:424–436

Deardorff J (1983) A multi-limit mixed-layer entrainment formulation. J Phys Oceanogr 13:988–1002

Deardorff J, Willis G, Stockton B (1980) Laboratory studies of the entrainment zone of a convectively mixed layer. J Fluid Mech 100:41–64

Dohan K, Sutherland B (2003) Internal waves generated from a turbulent mixed region. Phys Fluids 15(2): 488–498

Driedonks A (1982) Models and observations of the growth of the atmospheric boundary layer. Boundary-Layer Meteorol 23:283–306

Fedorovich E, Conzemius R, Mironov D (2004) Convective entrainment into a shear-free, linearly stratified atmosphere: bulk models reevaluated through large eddy simulations. J Atmos Sci 61:281–295

Fernando H (1991) Turbulent mixing in stratified fluids. Annu Rev Fluid Mech 23:455–493

Fernando H, Hunt J (1996) Some aspects of turbulence and mixing in stably stratified layers. Dyn Atmos Oceans 23:35–62

Fernando H, Hunt J (1997) Turbulence, waves and mixing at shear-free density interfaces. Part 1: a theoretical model. J Fluid Mech 347:197–234

Flamant C, Pelon J, Flamant P, Durand P (1997) Lidar determination of the entrainment zone thickness at the top of the unstable marine atmospheric boundary layer. Boundary-Layer Meteorol 83:247–284

Frehlich R (2001) Estimation of velocity error for Doppler lidar measurements. J Atmos Ocean Technol 18:1628–1639

Gryning SE, Batchvarova E (1994) Parametrization of the depth of the entrainment zone above the daytime boundary layer. Q J Roy Meteorol Soc 120:47–58

Haegeli P, Steyn D, Strawbridge K (2000) Spatial and temporal variability of mixed-layer depth and entrainment-zone thickness. Boundary-Layer Meteorol 97:47–71

Hannoun I, List EJ (1988) Turbulent mixing at a shear-free density interface. J Fluid Mech 189:211–234
Hunt J (1998) Eddy Dynamics and kinematics of convective turbulence, vol 513: bouyant convection in geophysical flows. Kluwer, Dordrecht, pp 41–82
Kalthoff N, Fiebig-Wittmaack M, Meixner C, Kohler M, Uriarte M, Bischoff-Gaux I, Gonzales E (2006) The energy balance, evapo-transpiration and nocturnal dew deposition of an arid valley in the andes. J Arid Environ 65:420–443
Kalthoff N, Adler B, Barthlott C, Corsmeier U, Mobbs S, Crewell S, Träumner K, Kottmeier C, Wieser A, Smith V, Girolamo PD (2009) The impact of convergence zones on the initiation of deep convection: a case study from cops. Atmos Res 93:680–694
Kim SW, Park SU, Moeng CH (2003) Entrainment processes in the convective boundary layer with varying wind shear. Boundary-Layer Meteorol 108:221–245
Kim SW, Park SU, Pino D, de Arellano JVG (2006) Parameterization of entrainment in a sheared convective boundary layer using a first-order jump model. Boundary-Layer Meteorol 120:455–475
Kottmeier C, Kalthoff N, Barthlott C, Corsmeier U, van Baelen J, Behrendt A, Behrendt R, Blyth A, Coulter R, Crewell S, di Girolamo P, Dorninger M, Flamant C, Foken T, Hagen M, Hauck C, Höller H, Konow H, Kunz M, Mahlke H, Mobbs S, Richard E, Steinacker R, Weckwerth T, Wieser A, Wulfmeyer V (2008) Mechanisms initiating deep convection over complex terrain during cops. Meteorol Z 17(6):931–948
Lammert A, Bösenberg J (2006) Determination of the convective boundary-layer height with laser remote sensing. Boundary-Layer Meteorol 119:159–170
Lenschow D, Stankov B (1986) Length scales in the convective boundary layer. J Atmos Sci 43(12):1198–1209
Lenschow D, Wyngaard J, Pennell W (1980) Mean field and second momentum budgets in a baroclinic convective boundary layer. J Atmos Sci 37:1313–1326
Lenschow D, Krummel P, Siems S (1999) Measuring entrainment, divergence, and vorticity on the mesoscale from aircraft. J Atmos Ocean Technol 16:1384–1400
Lenschow D, Wulfmeyer V, Senff C (2000a) Measuring second- through fourth-order moments in noisy data. J Atmos Ocean Technol 17:1330–1347
Lenschow D, Zhou M, Zeng X, Chen L, Xu X (2000b) Measurements of fine-scale structure at the top of marine stratocumulus. Boundary-Layer Meteorol 97:331–357
Linden P (1973) The interaction of a vortex ring with a sharp density interface: a model for turbulent entrainment. J Fluid Mech 60:467–480
Lothon M, Lenschow D, Mayor S (2006) Coherence and scale of vertical velocity in the convective boundary layer from a Doppler lidar. Boundary-Layer Meteorol 121:521–536
Lothon M, Lenschow D, Mayor S (2009) Doppler lidar measurements of vertical velocity spectra in the convective planetary boundary layer. Boundary-Layer Meteorol 132(2):205–226
McGrath J, Fernando H, Hunt J (1997) Turbulence, waves and mixing at shear-free density interfaces. Part 2. Laboratory experiments. J Fluid Mech 347:235–261
Melfi S, Spinhirne J, Chou SH, Palm S (1985) Lidar observations of vertically organized convection in the planetary boundary layer over the ocean. J Clim Appl Meteorol 24:806–821
Moeng CH (1998) Stratocumulus-topped atmospheric planetary boundary layer. In: Plate E, Fedorovich E, Viegas D, Wyngaard J (eds) Buoyant convection in geophysical flows, 1st edn. Kluwer, Dordrecht, p 491
Monin A, Obukhov A (1954) Basic laws of turbulent mixing in the atmosphere near the ground. Tr Akad Nauk SSSR Geofiz Inst 24(151):1963–1987
Nelson E, Stull R, Eloranta E (1989) A progostic relationsship for entrainment zone thickness. J Appl Meteorol 28:885–903
Nicholls S, Turton J (1986) An observation study of the structure of stratiform cloud sheets: Part II. Entrainment. Q J Roy Meteorol Soc 112:461–480
Pino D, de Arellano JVG, Duynkerke P (2003) The contribution of shear to the evolution of a convective boundary layer. J Atmos Sci 60:1913–1926
Seibert P, Beyrich F, Gryning SE, Joffre S, Rasmussen A, Tercier P (2000) Review and intercomparison of operational methods for the determination of the mixing height. Atmos Environ 34:1001–1027
Sorbjan Z (1990) Similarity scales and universal profiles of statistical moment in the convective boundary layer. J Appl Meteorol 29:762–775
Steyn D, Baldi M, Hoff R (1999) The detection of mixed layer depth and entrainment zone thickness from lidar backscatter profiles. J Atmos Ocean Technol 16:953–959
Strang E, Fernando H (2001) Entrainment and mixing in stratified shear flows. J Atmos Sci 428:349–386
Stull R (1973) Inversion rise model based on penetrative convection. J Atmos Sci 30:1092–1099
Sullivan P, Moeng C, Stevens B, Lenschow D, Mayor S (1998) Structure of the entrainment zone capping the convective atmospheric boundary layer. J Atmos Sci 55:3042–3064

Sun J, Wang Y (2008) Effect of the entrainment flux ratio on the relationship between entrainment rate and convective Richardson number. Boundary-Layer Meteorol 126:237–247

Tennekes H (1973) A model for the dynamics of the inversion above a convective boundary layer. J Atmos Sci 30:558–567

Tennekes H, Driedonks A (1981) Basic entrainment equations for the atmospheric boundary layer. Boundary-Layer Meteorol 20:515–531

Tucker S, Brewer WA, Banta R, Senff C, Sandberg S, Law D, Weickmann A, Hardesty R (2009) Doppler lidar estimation of mixing height using turbulence, shear, and aerosol profiles. J Atmos Ocean Technol 26:673–688

Turner J (1986) Turbulent entrainment: the development of the entrainment assumption, and its application to geophysical flows. J Fluid Mech 173:431–471

Van Zanten M, Duynkerke P, Cuijpers J (1999) Entrainment parameterization in convective boundary layers. J Atmos Sci 56(6):813–828

Wulfmeyer V, Behrendt A, Bauer H, Kottmeier C, Corsmeier U, Blyth A, Craig G, Schumann U, Hagen M, Crewell S, Girolamo PD, Flamant C, Miller M, Montani A, Mobbs S, Richard E, Rotach M, Arpagaus M, Russchenberg H, Schlüssel P, König M, Gärtner V, Steinacker R, Dorninger M, Turner D, Weckwerth T, Hense A, Simmer C (2008) Research campaign: the convective and orographically induced precipitation study. Bull Am Meteorol Soc 89:1477–1486

Yi C, Davis K, Berger B, Bakwin P (2001) Long-term observations of the dynamics of the continental planetary boundary layer. J Atmos Sci 58:1288–1299